Visualization and quantification of placental vasculature using MRI

Joanna Chappell[1], Magdalena Sokolska[2], Rosalind Aughwane[3], Alys R. Clark[4], Sebastien Ourselin[1], Anna L David[3,4], Andrew Melbourne[1]

1 School of Biomedical Engineering and Imaging Sciences (BMEIS), King's College London, 2 Department of Medical Physics and Biomedical Engineering, University College London Hospitals, UK.
3 Elizabeth Garrett Anderson Institute for Women's Health, University College London, UK. 4 Auckland Bioengineering Institute, New Zealand. 5 University College London Hospital NHS Foundation Trust, UK.

Abstract. Visualization of the placental vasculature in vivo is important for parameterization of placental function which is related to obstetric pathologies such as fetal growth restriction (FGR). However, most analysis of this vasculature is conducted ex vivo after delivery of the placenta. The aim of this study was to determine whether in vivo MRI imaging can accurately quantify the feto-placental vasculature, and to determine the impact of MRI contrast on its identification. Six different MRI contrasts were compared across 10 different cases. Image quality metrics were calculated, and analysis of vasculature segmentations performed. Measures of assessment included the vessel radius distribution, vessel connectivity and the identification of vessel loops. T_2 HASTE imaging performed the best both qualitatively, and quantitatively for PSNR and connectivity measures. A larger number of segmented branches at the smallest radii were observed, indicative of a richer description of the in vivo vascular tree. These were then mapped to MR perfusion fraction measurements from intra-voxel incoherent motion (IVIM) MRI. Mapped results were compared to measures extracted from gold-standard ex vivo micro-CT of the placenta and showed similar vessel density patterns suggesting that placental vessel analysis may be feasible in vivo.

Keywords: Placenta, Vasculature, Segmentation, Placental MRI

1 Introduction

Placental function with effective maternal-fetal oxygen and nutrient exchange is dependent on the development of a highly vascularized placental circulatory system. The placental vasculature is difficult to image in vivo with the majority of analyses in the literature completed ex vivo.

A well-functioning placenta is vital for healthy fetal growth and development. Many complications of pregnancy such as fetal growth restriction (FGR) and pre-eclampsia are linked to placental insufficiency and inadequate vasculogenesis and angiogenesis.

FGR in the UK leads to 2/3 of stillbirths [1] and earlier clinical knowledge of the placental function would aid in clinical decision making. In FGR placentas, there appears to be reduced vascular branching and narrower vessels leading to a significant reduction in uteroplacental blood flow and hence oxygen and nutrient exchange [2].
Ultrasound is the most utilized imaging technique during pregnancy, providing a low cost and accessible option, able to assess the uteroplacental blood flow and fetal vascular impedance [3]. However, MRI has been increasingly used to investigate pregnancy complications, and can measure variations in the placental structure as well as provide blood and oxygenation metrics [1], [4].

Placental vasculature modelling is not a new concept and has been completed across vascular scales utilizing different imaging methods. Differences in the placental vasculature have been observed ex vivo using micro-CT [5] and at the microstructural level using confocal laser scanning [6]. Evidence suggests that placental vasculature does change ex vivo with the cessation of uteroplacental blood circulation [2]. Additionally, ex vivo imaging does not provide immediate information for patient specific decision making.

MRI provides a solution to this, by segmenting the vasculature trees in combination with diffusion and relaxation-based perfusion and oxygenation measurements. However, visualization of blood vessels using MRI is difficult and can vary with different MRI contrasts. This study aims to assess the feasibility of extracting placental vasculatures from in vivo MRI, using different contrasts, and to quantify the nature of vascular networks extracted from this in vivo imaging.

1.1 MRI acquisitions and differing contrasts

Relaxation times (T_1 and T_2) describe how long the tissue takes to return to equilibrium after a radiofrequency (RF) pulse. T_1 and T_2 depend on different tissues. Fluids have long T_1 (1500-2000ms), water-based tissues are usually mid-range (400-1200ms) and fat tissues are usually short (100-150ms). In general, images have contrast which depends on proton density, T_1 or T_2. The T_1 weighted MRI enhances the appearance of fatty tissue, while T_2-weighted images enhance the signal of the water [7]. T_2* is the transversal relaxation time constant within gradient-echo MRI using a long repetition time, long echo time and low flip angle, which can be used for detecting changes in oxygen saturation [8].

MRI HASTE (Half-Fourier Acquisition Single-shot Turbo Spin Echo) is a rapid imaging technique to acquire T_2-weighted images, utilizing a single-shot acquisition and half-Fourier sampling to reduce acquisition time. It is particularly useful in maternal and fetal MRI due to its fast acquisition time reducing the effect of fetal motion [9].

Diffusion-weighted imaging (DWI) is common in medical MRI and particularly in placental imaging measuring the displacement of the water molecules within the tissue over a time interval. The diffusion sensitivity can be characterized by the b-value, which reflects the strength and timing of the gradients used to create the DWIs [10].

Intravoxel incoherent motion (IVIM) MRI is an imaging method to separate the vascular and nonvascular components of the anatomy. IVIM measures the microcirculation in the capillary bed and has shown sensitivity to multiple pregnancy complications with

fetal and maternal origins including FGR [11]. In this way IVIM measurements can provide a measurement of vascular density within the placenta, even when the vessel network is not resolvable.

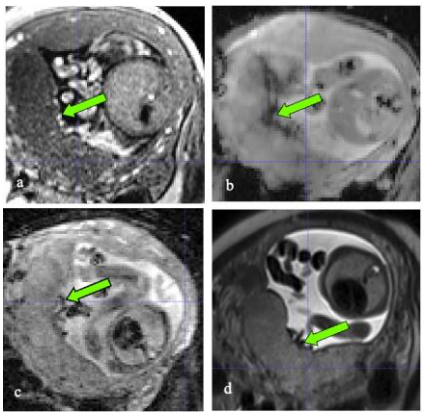

Fig. 1. The figure shows the different MRI contrast images for a pregnancy FGR. Shown are (a) T_1, (b) T_2*, (c) IVIM (at b-value =0 s/mm^2), and (d) HASTE. Major blood vessels are identified by arrows. A visual difference in the appearance of the vasculature can be observed.

2 Methods

2.1 Data acquisition

MRI data from 10 pregnant patients (6 with FGR (estimated fetal weight < 10th centile) and 4 normally grown fetuses) at 24+2-33+6 GA was acquired with a 1.5T Siemens Avanto under free-breathing [12]. The voxel resolution was 1.9 x 1.9 x 6 mm. The data was acquired as a combination of 7 b-values and 9 echo-times. IVIM was acquired at b-values (0,50,100,150,200,400,600 s/mm^2) and T_2 relaxometry at echo times (77,90,120,150,180,210,240,270,300ms). To allow T_2 fitting, all echo times were acquired at b-value 0 and all b-values at 96 milliseconds. In addition, data were acquired at b-values 50 and 200 for t=81, 90, 120, 150,180, 210 and 240 milliseconds. The total acquisition time was approximately 20 minutes making the data acquisition tolerable for subjects. This integrated acquisition provides an improved separation of long T2 compartments with different incoherent motion properties which integrate the effects of diffusion, perfusion and oxygenation [13]. The study was approved by the UK National Research Ethics Service and all participants gave written informed consent (London – Hampstead Research Ethics Committee, REC reference 15/LO/1488). All the data were anonymized. All patients had T_1 and HASTE contrasts, 6 had T_2*, 3 had additional T_2 HASTE and 3 had additional IVIM diffusion imaging.

2.2 Image quantification metrics

Images were quantified with the following measures:

Signal-to-noise ratio (SNR). Measured by taking the mean of a high-intensity region of interest and dividing by the standard deviation of the region of noise outside of the imaged object [14].

Peak signal-to-noise ratio (PSNR). Is an expression of the ratio between the maximum values of signal and the power of the distorting noise that affects the quality of the image, it is calculated as [14]

$$\mathrm{PSNR} = 20\log_{10}\left(\frac{MAX_f}{\sqrt{MSE}}\right), \tag{1}$$

where MAX_f is the maximum signal and MSE is the mean squared error.

Structural similarity image metric (SSIM) measures the local structural similarity, by using a correlation between the quality and the perception of the human visual system. Instead of using traditional error summation methods, the SSIM models image distortion and contrast distortion [14].

Entropy is a statistical measure of the randomness that can be used to characterize the texture of the input image. It is a quantitative measure of the information transmitted in the image. It is defined as:

$$\mathrm{Entropy} = -\sum_{i=1}^{n} p \cdot \log_2 p \tag{2}$$

where p contains the normalized histogram counts [15]–[17].

2.3 Quantification of vessel segmentation

Manual segmentations of the vessel trees were carried out on each image contrast and the resultant vascular tree quantified using:

Maximum and minimum radii from the manual segmentations were calculated alongside the volume of vessels segmented. These were plotted against each of the contrasts and visualized in 3D using VesselVio [18].

Connectivity of the segmentations was quantified using skeletonization; the branch points and vessel lengths were calculated. From this the connectivity index was assessed as total length of the vessel network divided by the total area of the segmentation. The higher the connectivity index the more interconnected the vessels are within the segmentation [19].

Looping of the segmentations was quantified by detecting the connected components in a closed or distinct loop [20].

2.4 Statistics

The difference between each metric described in Section 2.3 and 2.4 that was derived from each MRI contrast was assessed statistically using a 2 tailed t-test with a p value of <0.05 defined as statistically significant.

2.5 Segmentation performance evaluation

In order to evaluate the manual segmentations, we compare them to properties of the fetal vasculature from a gold standard ex vivo perfused placenta that had undergone micro-CT examination. Data from a single placenta was acquired from a woman undergoing elective term caesarean section following uncomplicated pregnancy. The placenta was perfused with Microfil and imaged over the whole volume via micro-CT with isotropic voxel size of 116.5μm [2]. The placental vasculature was extracted and analyzed using the same analysis as for the MRI [5].
The MRI and CT vessel segmentations and networks were analyzed. The vessel trees from the HASTE MRI and micro-CT were skeletonized and vessel endpoints extracted. The local vessel density was then measured distal to each endpoint. In the case of MRI, vessel density is estimated from IVIM-MRI weighted by a Gaussian distribution from each skeleton endpoint with a 3 pixels standard deviation. The distance of each endpoint from the umbilical cord insertion point is measured. In the case of the micro-CT, the vessel segmentation is thresholded at a vessel radius corresponding to the start of the placental stem arteries. Subsequently the local vessel density is measured at each of these end-points. Vessel density is estimated as the volume of segmented vessel in a region close to the corresponding endpoint, with 2.5 pixels radius. Distances of each end-point from the umbilical cord insertion are measured. A comparison was made between the results of the MRI and micro-CT vessel density measurements and how they vary with distance from cord insertion.

3 Results

Figure 2 shows the vessel segmentations obtained for each of the imaging contrasts for one case, the segmentation quantification of the radii and volume is stated.

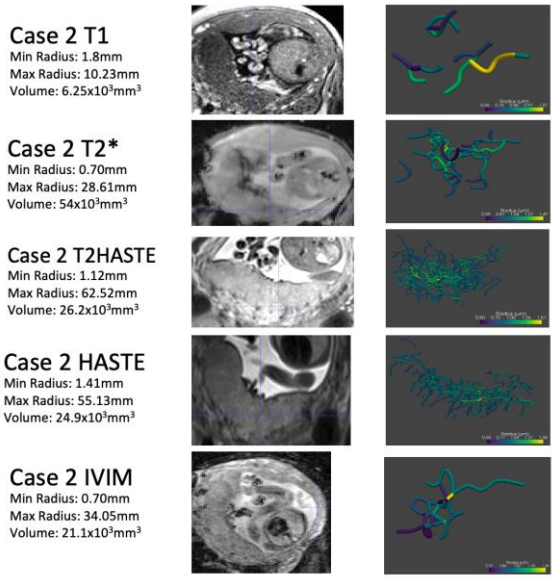

Fig. 2. The contrast comparison for the visualization of the vessels alongside the 3D model of the segmented vessels from VesselVio. Maximum (Max) and minimum (Min) radii of identified vessels, as well as total volume of vessels is stated. Colorbars represent vessel radius.

Figure 3 shows how the distribution of radii from each of the segmentations varies between imaging contrasts.

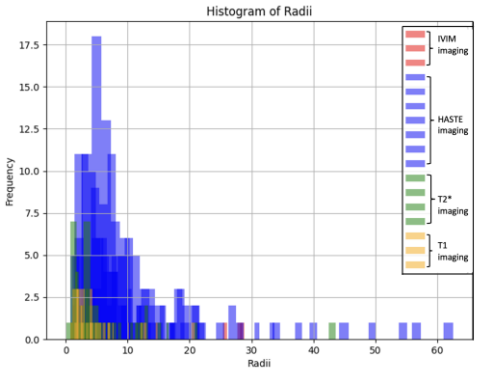

Fig. 3. The spread and the histogram of the radii showing the density spread for each of the contrasts for all the cases and across all of the image contrasts.

Values for the four image quality metrics are shown in Table 1. Only the PSNR was significant between the diffusion IVIM imaging and the HASTE imaging. The volume

of vessels identified was higher for the IVIM imaging, the connectivity was significantly higher for the HASTE imaging than the IVIM, T_1 and T_2*. Identified looping increased with increased connectivity.

Table 1. Combined results from the image quality metrics and the segmentation properties

	HASTE	T_2 HASTE	T_1	T_2*	IVIM
Image Quality Metrics					
PSNR	30.9±0.79	29.2±2.13	39.9±0.79	37.5±2.13	42±1.77
SNR	19.9±0.010	20.0±0.010	19.9±0.026	20.0±0.030	20.0±0.040
Entropy	6.72±0.003	6.72±0.002	6.72±0.004	6.72±0.005	6.71±0.006
SSIM	0.09±0.0002	0.09±0.0002	0.09±0.0005	0.09±0.0006	0.09±0.0006
Segmentation Properties					
Volume (mm^3)	9596.60	26210.68	10578.8	34825.5592	55050.9
Max Radius (mm)	44.41 ± 13.78	56.3 ± 8.803	17.84 ± 14.8	18.6 ± 6.88	28.45 ± 10.2
Min Radius (mm)	1.41 ± 0.46	1.81 ± 0.98	1.06 ± 0.54	0.707 ± 0.23	1.81 ± 0.50
Connectivity	49.36±3.96	56.03±6.94	40.03 ±6.57	51.34 ± 6.94	41.05±4.33
Looping	25±14.5	48.5 ± 16.3	8±2	11.5 ±2.5	6 ±2

3.1 Validation from micro-CT

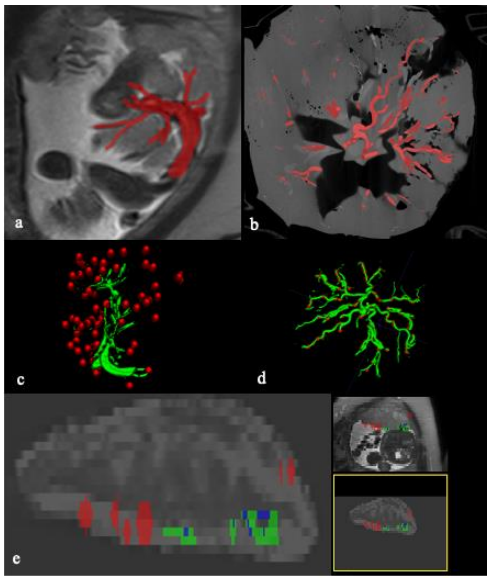

Fig. 4. Comparison of vasculature segmentations from MRI and Micro-CT: Sagittal slice from HASTE MRI with the segmentation of the vasculature overlayed in red (A), Micro-CT with the segmented vasculature in red (B). 3D skeletons of the segmentations in green with the red end-points for the MRI and Micro-CT respectively (C and D). IVIM perfusion density map, with end point locations identified in red, segmentation in green and skeleton in blue (E).

Figure 4 compares image segmentations from MRI and micro-CT and Figure 5 shows the relationship between vessel density and distance from umbilical insertion point. Both MRI data and micro-CT data show a significant negative trend of vessel density with distance. The agreement between these two datatypes is consistent with previous ex vivo literature and demonstrates that MRI can extract comparable relationships in vivo by the combination of high-resolution structural imaging and IVIM imaging.

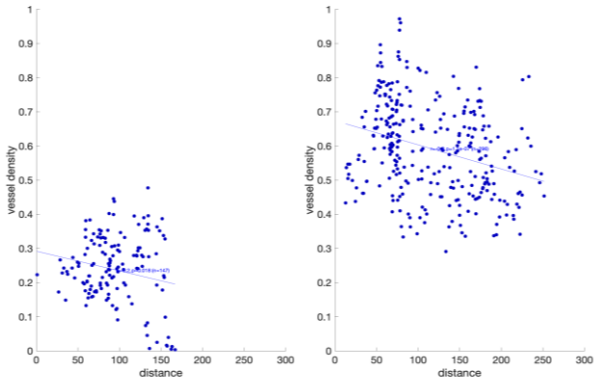

Fig. 5. The vessel density at the end points of the vessel segmentations for the MRI on the left and micro-CT data on the right.

4 Discussion

This work has shown that compared with other MRI protocols T_2 HASTE images provide a better visualization of the feto-placental vasculature, with the quantitative measures for PSNR and connectivity being significantly higher than the other contrasts. Vessel segmentations can be combined with IVIM MRI data to allow a coupled analysis of vessel density. Validation with ex vivo Micro-CT data showed that coupled segmentations from HASTE and markers of vessel density from IVIM imaging show similar spatial trends in terms of the vessel density to a gold standard ex vivo segmentation.

HASTE cases have lower PNSR than diffusion models (IVIM and DECIDE). The other image quality metrics were not significantly different. There are limitations to the use of the PSNR and SNR as both calculations make assumptions as to the image intensity reducing the accuracy of the parameters. This could be due to the SSIM being correlated with the HVS color model and all the images being greyscale. The entropy values were very similar throughout, although the HASTE often had the lowest standard deviation, implying a reduced apparent randomness.

The segmented vessel volume was higher in the DECIDE and IVIM cases, likely related to the PSNR, with the diffusion models being lower and vasculature being harder to observe clearly. Volumes were lower for the HASTE imaging despite visual

appearance of more branching observed in these images (Fig. 2). With HASTE imaging, a higher number of branching units can be observed (Fig. 2 and 3) with radii distributions with higher median and larger numbers of smaller vessels than any other contrast. The connectivity of the segmentations calculated for the T_2 imaging, HASTE and star, gave the highest values with the T_1 imaging and diffusion imaging having similar averages.

Vessel looping was highest in the HASTE contrasts most likely due to greater value of branching segments in comparison to the T_1 and the diffusion imaging. The connectivity and lopping parameters correlated positively as more branches led to higher looping. However, the looping could be more accurately detected using a cycle detection algorithms like depth-first search (DFS) or Tarjan's algorithm.

One limitation of these measures is that they are an incomplete assessment of the quality of the imaging and the quality of the resulting segmentation. The manual segmentations are possibly limited by user-error, and are subjective, but were required in this study to ensure vascular connectivity. However, in combination, the vessel segmentation and image quality measures have the potential to be combined to form a unified cost-function of image quality and vessel extraction. This may eventually help automate the vessel segmentation process.

Comparison with micro-CT data showing vessel density against distance from the umbilical cord insertion for MRI and ex vivo micro-CT (Fig. 5) indicates that both show a negative correlation. This result is comparable to previously published ex vivo work in the placenta [2]. The correlation is not as strong in the MRI as the resolution of vessel branching is greatly reduced due to a reduced resolution and quality of segmentation but the substitution of vessel density with IVIM perfusion density allows sub-voxel inferences to be made.

5 Conclusion

In conclusion, we have shown that feto-placental vascular networks can be extracted from in vivo MRI imaging data. Comparison with micro-CT data indicates that it is possible to obtain in vivo MRI data that with correspondence to subsequent post-delivery analysis. Our findings suggest that more detailed placental analysis may be possible in vivo, supporting the translation of advanced placental imaging technology to the clinic.

References

[1] R. Aughwane, *et al.*, “Placental MRI and its application to fetal intervention,” *Prenat Diagn*, vol. 40, no. 1, pp. 38–48, Jan. 2020, doi: 10.1002/pd.5526.

[2] M. Byrne *et al.*, “Structure-function relationships in the feto-placental circulation from in silico interpretation of micro-CT vascular structures,” *J Theor Biol*, vol. 517, May 2021, doi: 10.1016/j.jtbi.2021.110630.

[3] E. A. Turk *et al.*, “Placental MRI: developing accurate quantitative measures of oxygenation HHS Public Access,” *Top Magn Reson Imaging*, vol. 28, no. 5, pp. 285–297, 2019, doi: 10.1097/RMR.0000000000000221.

[4] A. Melbourne, “On the use of multicompartment models of diffusion and relaxation for placental imaging,” *Placenta*, vol. 112. W.B. Saunders Ltd, pp. 197–203, Sep. 01, 2021. doi: 10.1016/j.placenta.2021.07.302.

[5] W. M. Tun, *et al.*, “Differences in placental capillary shear stress in fetal growth restriction may affect endothelial cell function and vascular network formation OPEN”, doi: 10.1038/s41598-019-46151-6.

[6] G. J. Burton *et al.*, “Pathophysiology of placental-derived fetal growth restriction,” *American Journal of Obstetrics and Gynecology*, vol. 218, no. 2. Mosby Inc., pp. S745–S761, Feb. 01, 2018. doi: 10.1016/j.ajog.2017.11.577.

[7] M. Sinding *et al.*, “Prediction of low birth weight: Comparison of placental T2* estimated by MRI and uterine artery pulsatility index,” *Placenta*, vol. 49, pp. 48–54, Jan. 2017, doi: 10.1016/J.PLACENTA.2016.11.009.

[8] D. Kawahara *et al.*, “T1-weighted and T2-weighted MRI image synthesis with convolutional generative adversarial networks,” *Reports of Practical Oncology and Radiotherapy*, vol. 26, no. 1, pp. 35–42, 2021, doi: 10.5603/RPOR.a2021.0005.

[9] R. C. Semelka, *et al.* “HASTE MR Imaging: Description of Technique and Preliminary Results in the Abdomen”, doi: 10.1002/jmri.1880060420.

[10] R. Fusco, *et al.*, “A comparison of fitting algorithms for diffusion-weighted MRI data analysis using an intravoxel incoherent motion model,” *Magn Reson Mater Phy*, vol. 30, pp. 113–120, 2017, doi: 10.1007/s10334-016-0591-y.

[11] Y. Liao *et al.*, “Journal Pre-proof Detecting abnormal placental microvascular flow in maternal and fetal diseases based on flow-compensated and non-compensated intravoxel incoherent motion imaging,” p. Placenta, 2022, doi: 10.1016/j.placenta.2022.01.010.

[12] R. Aughwane *et al.*, “Magnetic resonance imaging measurement of placental perfusion and oxygen saturation in early-onset fetal growth restriction”, doi: 10.1111/1471-0528.16459.

[13] A. Melbourne *et al.*, “Separating fetal and maternal placenta circulations using multiparametric MRI,” 2016. [Online]. Available: https://www.researchgate.net/publication/324079328

[14] E. Plenge, *et al.*, “LNCS 8151 - Super-Resolution Reconstruction Using Cross-Scale Self-similarity in Multi-slice MRI,” 2013. [Online]. Available: http://www.bigr.nl/

[15] Q. Ji, *et al.*, “A novel, fast entropy-minimization algorithm for bias field correction in MR images.”

[16] R. Obuchowicz, *et al.*, “Magnetic Resonance Image Quality Assessment by Using Non-Maximum Suppression and Entropy Analysis,” *Entropy 2020, Vol. 22, Page 220*, vol. 22, no. 2, p. 220, Feb. 2020, doi: 10.3390/E22020220.

[17] D. Y. Tsai, *et al.*, “Information entropy measure for evaluation of image quality,” *J Digit Imaging*, vol. 21, no. 3, pp. 338–347, Sep. 2008, doi: 10.1007/s10278-007-9044-5.

[18] J. R. Bumgarner *et al.*, “Open-source analysis and visualization of segmented vasculature datasets with VesselVio”, doi: 10.1016/j.crmeth.2022.100189.

[19] J. Zhang, *et al.*, “Techniques and Algorithms for Hepatic Vessel Skeletonization in Medical Images: A Survey,” *Entropy*, vol. 24, no. 4. MDPI, Apr. 01, 2022. doi: 10.3390/e24040465.

[20] K. Li, *et al.*, “Optimal surface segmentation in volumetric images - A graph-theoretic approach,” *IEEE Trans Pattern Anal Mach Intell*, vol. 28, no. 1, pp. 119–134, Jan. 2006, doi: 10.1109/TPAMI.2006.19.